33RD CONGRESS
OF THE INTERNATIONAL COUNCIL
OF THE AERONAUTICAL SCIENCES
STOCKHOLM, SWEDEN, 4-9 SEPTEMBER, 2022

ICAS 2022 SWEDEN

TRANSONIC NACELLE DESIGN FOR FUTURE MEDIUM RANGE AERO-ENGINES

B.D.J Schreiner[1], D.G. MacManus[1], F. Tejero*[1], F. Sanchez-Moreno[1] & C. Sheaf[2]

[1]Centre for Propulsion and Thermal Power Engineering, School of Aerospace, Transport and Manufacturing, Cranfield University, Bedfordshire, MK43 0AL, United Kingdom
[2]Rolls Royce Plc., P.O. Box 31, Derby, DE24 8BJ, United Kingdom

Abstract

It is expected that future civil aero-engines will operate at low specific thrust and high-bypass ratios to improve propulsive efficiency. This may result in an increment in fan diameter and associated weight and nacelle drag penalties. For this reason, these new architectures may use compact nacelles to meet the benefits of the new engine cycles. The aim of the current work is to evaluate the aerodynamic design and performance of compact nacelles for medium range, single-aisle aircraft with a cruise Mach number of M = 0.80. This work encompasses the 3D multi-point, multi-objective optimisation of nacelles by considering cruise conditions as well as a range of off-design requirements such as an increased cruise Mach number, a windmilling engine-out diversion scenario and a windmilling end-of-runway case at high-incidence. This paper also explores the robustness and sensitivity of selected designs to flight Mach number (M), massflow capture ratio (MFCR) and angle of attack (AoA). The limits of the feasible design space for this new design challenge are identified. It is concluded that relative to a conventional aero-engine nacelle, the nacelle length (L_{nac}/r_{hi}) can be reduced by approximately 13% with a mid-cruise drag reduction of 5.8%, whilst maintaining an acceptable aerodynamic performance at off-design conditions.

Keywords: nacelle, transonic, UHBPR, multi-objective optimisation

1. Introduction

Flightpath 2050 [1] has defined very ambitious aerospace performance targets. Relative to a year-2000 aircraft it aims for reductions of 75% in fuel-burn, 80% in landing/take-off emissions and 65% in perceived noise. To meet these challenges, different advanced optimisation methods[2, 3], flow control technologies [4, 5] or innovative aerodynamic systems [6] are considered. In this respect, a range of propulsion configurations are being investigated such as Ultra-high bypass ratio (UHBPR) aero-engines [7] or boundary layer ingestion [8]. For future UHBPR architectures, it is expected that the fan diameters will increase to meet the specifications of the new engine cycles [7]. Therefore, the nacelle wetted area may increase if current design rules are used. This will result in large low-specific thrust engines with penalties in nacelle drag, overall weight and powerplant-airframe integration [9, 10]. For this reason, it is anticipated that future UHBPR aero-engines will mount compact nacelles to retain the expected aerodynamic benefits of these new configurations [11].

There is very limited information in the open literature regarding the feasible design space of compact aero-engine nacelles for medium range applications with a mid-cruise flight Mach number of M_{cruise} = 0.80. The majority of the studies for UHBPR aero-engine nacelles are focused in long-range applications with M_{cruise} = 0.85. For example, Tejero *et al.* developed a fully integrated nacelle design and optimisation capability for isolated 2D axisymmetric [12], isolated 3D non-axisymmetric [13] and installed [14] architectures. It was concluded that for isolated configurations, the nacelle drag

could be reduced by approximately 8.5% when the nacelle length (L_{nac}) normalised with the highlight radius (r_{hi}) was reduced from L_{nac}/r_{hi} = 3.6 to 3.1. These two nacelles were representative of a conventional architecture and a future civil aero-engine, respectively. For installed configurations, a similar benefit was obtained for forward installation positions because of the relatively low installation penalties. Conversely, the benefits were eroded by a factor of approximately three for close-coupled positions due to the larger installation penalties of compact aero-engine nacelles with respect to conventional ones. Savelyev *et al.* [15] developed a tool for for the design and optimisation of nacelle/intake/exhaust systems to minimise the powerplant thrust losses. For a cruise Mach number of 0.85, the process resulted in an increment of the effective thrust of 1.5% with respect to a reference configuration. Schreiner *et al.* [16] carried out a set of independent 2D axisymmetric multi-point, multi-objective optimisations within the range of $2.5 < L_{nac}/r_{hi} < 4.3$. The process included different operating conditions of the cruise segment, e.g. mid-cruise conditions and an increase Mach number as well as different windmilling scenarios such as diversion or cruise engine-out. It was concluded that compact aero-engine nacelles are more sensitive to off-design conditions and, as such, they should be included in the optimisation process to ensure that the process yields aerodynamic robust configurations. It was quantified that a length reduction from L_{nac}/r_{hi} = 4.3 to 3.1 resulted in a mid-cruise nacelle drag benefit of approximately 10%.

Few previous investigations have been focused on the design of aero-engine nacelles for medium-range application with M_{cruise} = 0.80. These studies mainly aimed to develop methods and tools for the design and optimisation of UHBPR nacelles. However, they were not used to understand and investigate the geometrical feasible design space for these architectures. For example, Fang *et al.* [17] developed a framework that encompassed numerical simulations, a surrogate-based optimisation strategy based on the Kriging interpolation method [18] and a genetic algorithm [19]. It was used for the MOO of a 3D non-axisymmetric nacelle with $L_{nac}/r_{hi} \approx 3.5$. The optimisation was carried out for two operating conditions in which the cruise Mach number was fixed to M_{cruise} = 0.80 and the angle of attack was set to AoA = 0° and 4°. Relative to a reference, the method yielded an optimal nacelle with 4% nacelle drag reduction at AoA = 4° while maintaining a similar drag value at the low incidence angle of AoA = 0°. Silva *et al.* [20] carried out a multi-point aerodynamic design investigation of an ultra high-bypass-ratio turbofan engine with L_{nac}/r_{hi} = 3.0. The process used mid-cruise (M_{cruise} = 0.80) as well as off-design conditions such as end-of-runway high angle of attack or crosswind. The challenges of designing robust configurations across all the flight envelope were highlighted and it was concluded that the crosswind scenario limits the feasible design space.

The aim of the current work is to evaluate the aerodynamic design and performance of compact nacelles for medium range application with M_{cruise} = 0.80. The novelty of this paper lies in the identification of the feasible design space for this new nacelle design challenge. The work encompasses the 3D multi-point, multi-objective optimisation of nacelles by considering cruise conditions as well as a range of off-design requirements such as an increased cruise Mach number, an engine-out diversion scenario and an engine-out end-of-runway case. This paper also explores the robustness and sensitivity of selected designs to flight Mach number (M), massflow capture ratio (MFCR) and angle of attack (AoA).

2. Methodology

This work uses a well established numerical approach for the analysis, design and optimisation of aero-engine nacelles [12, 13, 21]. It is based in a CFD-based workflow with a fully parametric definition of the aero-engine housing components [22, 23], RANS numerical simulations [24, 25], a thrust-drag bookkeeping capability to extract the nacelle drag [26] and a genetic algorithm to perform multi-point multi-objective optimisations [19].

The intuitive Class-Shape Transformation method is used for the intake, nacelle and exhaust definition. Seven intuitive parameters are used to define each nacelle aero-line: r_{hi}, L_{nac}, r_{te}, r_{if}, f_{max}, r_{max} and β_{nac} (Figure 1a). Besides, the intake angles of scarf (θ_{scarf}) and droop (θ_{droop}) are also para-

metrically defined [27]. The 3D non-axisymmetric aero-engines are controlled with 5 aero-lines (ψ = 0°, 45°, 90°, 135° and 180°) (Figure 1b). This results in a high-dimensional space with 37 design parameters to control the shape of 3D non-axisymmetric aero-engine nacelles. Within the context of this study, the intuitive variables of θ_{scarf}, θ_{droop}, r_{hi}, L_{nac} and r_{te} are fixed during the multi-point optimisation routine. As such, only the variables r_{if}, f_{max}, r_{max} and β_{nac} vary, which reduces the optimisation degrees of freedom to 20. A generic conical exhaust is used to generate a representative post-exit streamtube upon which the nacelle drag is extracted [27].

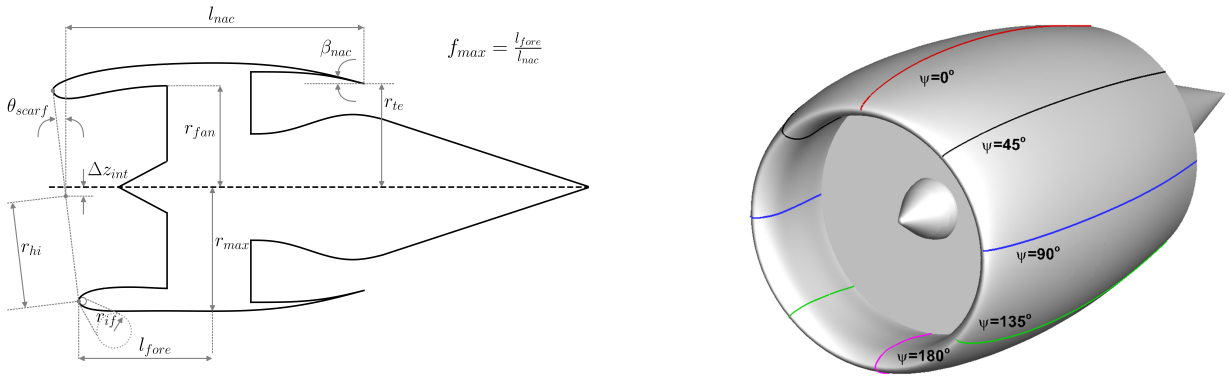

(a) Intuitive variables

(b) 3D azimuthal control

Figure 1 – Fan cowl and intake geometric parameters for a drooped and scarfed nacelle and azimuthal control line. Adapted from [27]

The overall method is coupled with an automated mesh generation tool to create a multi-block structured grid [25] (Figure 2a). The compressible steady Favre-averaged Navier-Stokes equations are solved with a density-based solver. The k-ω SST model turbulence closure [28, 29] is used with the Green-Gauss node based scheme [30] and a second order spatial discretization. Sutherland's law is applied for the calculation of the viscosity [31]. The computational approach has been validated for a wide range of operating conditions within the cruise segment as well as for different off-design windmilling scenarios [21]. The farfield is defined with pressure-farfield boundary conditions in which the Mach number and static tempeature and pressure are set. The fan face is modelled with a pressure-outlet boundary condition with a targeted massflow to obtain the specified operating massflow capture ratio (MFCR). The exhaust inlet uses a pressure-inlet boundary condition in which freestream total pressure and temperature are imposed (Figure 2b). The first layer height is adjusted to obtain $y^+ = 50$ so wall-functions are used for the boundary layer calculations to reduce the computational cost [32]. The same strategy has been employed in previous studies. A grid sensitivity study was previously carried out in which 3 different mesh sizes with 400k, 800k and 1,600k were considered [13]. For the reference mesh with 800k cells, the grid convergence index (GCI) as described Roache [33] depicted a GCI of 2.5% and has been used for this investigation.

Relative to previous nacelle design studies [12, 13], the optimisation method is extended from a solely regression algorithm to also include the mixture of a regression and classification approach. The regression element is used to minimize the nacelle drag at key conditions such as cruise as well as the increased Mach number cruise condition. The classification capability is used to evaluate designs based on an acceptability threshold for a flow field feature. In this study the classification is based on the extent of the local boundary layer separation at the off-design windmilling conditions. Separation extent is evaluated along three aero-lines ($\psi = 0°, 45°$ and $90°$ in Figure 1b). The sign of the axial wall shear term ($\tau_{w,x}$) is examined to determine the fraction of nacelle length that has reverse flow. The multi-point, multi-objective optimisation routine is driven with the genetic algorithm NSGA-II, proposed by Deb *et al.* [19], due to its capability for global optimisation in non-linear problems. The process starts with a design space exploration from a Latin Hypercube Sampling (LHS) [34] to efficiently populate the relatively large design space considered with 20 degrees of freedom. All the nacelles are evaluated with CFD across all the different operating conditions considered. For the

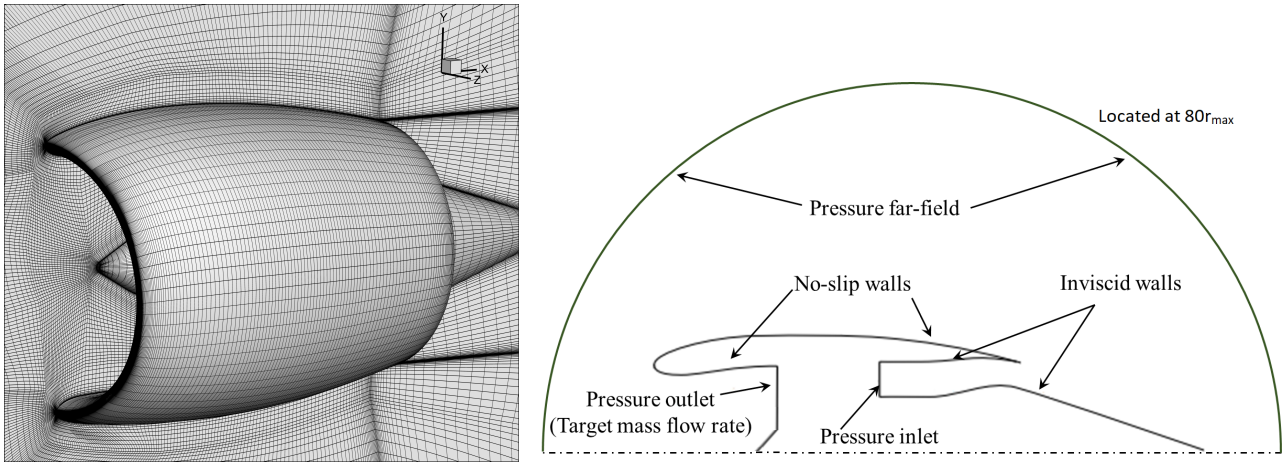

(a) Nacelle surface mesh

(b) Definition of boundary conditions

Figure 2 – Overview of the computational approach

subsequent generations of the NSGA-II algorithm, the nacelle drag evaluations are also performed with numerical simulations.

3. Results and analysis

This study aims to quantify the expected benefits of compact aero-engine nacelles for medium-range applications with cruise flight Mach number of 0.80 with respect to in-service architectures. For this purpose, the effect of the normalised nacelle variable of (L_{nac}/r_{hi}) is investigated. Three independent multi-point, multi-objective optimisations are carried out with different L_{nac}/r_{hi}. The longest aero-engine nacelle of L_{nac}/r_{hi} (or also referred as $L_{nac}/r_{hi} = L_{ref}$) is used as a representative configuration and reference upon which the nacelle drag changes for the other architectures ($L_{nac}/r_{hi} = 0.87 \cdot L_{ref}$ and $0.81 \cdot L_{ref}$) are quantified.

Four different operating conditions were used (Table 1). These are representative of mid-cruise conditions ($C_{D-cruise}$), sensitivity to an increased Mach number within the cruise segment (C_{D-iM}), diversion windmilling scenario ($C_{D-diversion}$) and windmilling end-of-runway (EoR) at high-angle of attack of AoA = 20° [35]. For this study, the two first operating points, i.e. $C_{D-cruise}$ and C_{D-iM}, are considered as regression functions in which the nacelle drag is minimised. This is to ensure that the derived configurations have low fuel burn. The windmilling diversion scenario is initially classified in terms of a separation threshold (L_{sep}/L_{nac} < 0.10) and, if this requirement is met the nacelle drag ($C_{D-diversion}$) is minimised. This aims to maximise the ETOPS range in case of one-engine shut-down. The last conditions, i.e. EoR, is treated as a classification condition in which the maximum acceptable flow separation extension was set to L_{sep}/L_{nac} < 0.10.

Name	Mach	MFCR	AoA	Type
$C_{D-cruise}$	0.80	0.70	4.5	Regression
C_{D-iM}	0.82	0.70	4.5	Regression
$C_{D-diversion}$	0.60	< 0.5	4.5	Classification/Regression
EoR	0.25	< 0.5	20.0	Classification

Table 1 – Flight conditions evaluated during the multi-point, multi-objective routine

The current nacelle design and optimisation problem is very challenging due to the associated non-linearity of this problem, in which the aerodynamics of the nacelle at the different 4 flight conditions are notable different. The mid-cruise and increased Mach number conditions are characterized by a

controlled flow acceleration around the nacelle lip which usually terminates in a well defined shock-wave at the nacelle crest within its top-half (Figure 3a). For the windmilling diversion scenario, the flow acceleration around the lip is stronger due to the reduction in the operating MFCR. It results in a shock located on the forebody near the highlight with a higher pre-shock Mach number than for the cruise conditions (Figure 3b). Lastly, the windmilling end-of-runway case at high-angle-of-attack is characterized by diffusion driven separation over the nacelle aft body at high incidences. For this reason, this flight condition is treated as a classification metric to ensure that the flow is attached within the defined threshold.

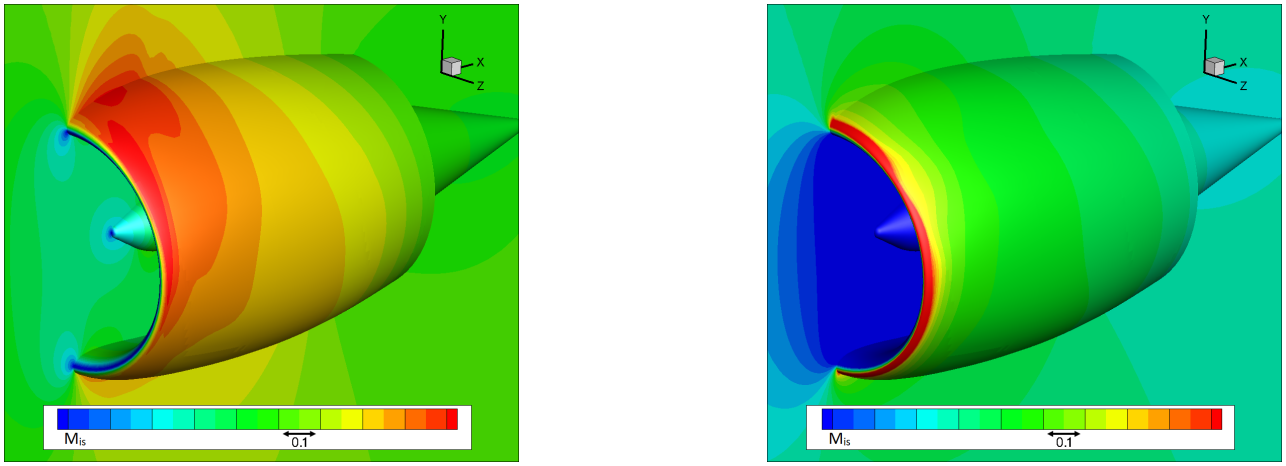

(a) Mid-cruise

(b) Windmilling diversion

Figure 3 – Example of flow-field for two operating conditions evaluated during the multi-point, multi-objective optimisation

As previously described the multi-point, multi-objective optimisation starts with a design space exploration (DSE) based on a Latin Hypercube Sampling. Approximately 400 aero-engine nacelles are evaluated with CFD during the DSE. Following generations within the NSGA-II algorithm are composed by 200 individuals. The hypervolume indicator [36] is monitored during the optimisation routine as the design process is stopped once there are changes in the hypervoulume below 1% within 3 consecutive generations.

As an example of the outcome of the multi-point MOO, Figure 4 presents the Pareto front for the baseline aero-engine configuration with $L_{nac}/r_{hi} = L_{ref}$. As the optimisation routine considers three regression function, the Pareto front is a 3D surface. To aid with the visualization, it is initially projected into the $C_{D-cruise}$ - $C_{D-diversion}$ space and colored by C_{D-iM} (Figure 4a). It clearly highlights the non-linear correlation for $C_{D-cruise}$ - $C_{D-diversion}$ which emphasizes the needs to use this diversion scenario during the optimization routine. Conversely, the Pareto front projected in the $C_{D-cruise}$ - C_{D-iM} space (Figure 4b) reveals a strong linear correlation between both metrics. However, this linear correlation does not arise for compact configurations (e.g. $L_{nac}/r_{hi} = 0.87 \cdot L_{ref}$) as described below which suggest that the nacelle drag sensitivity to Mach number (C_{D-iM}) is a metric required in an optimisation process for UHBPR aero-engine nacelles. Four designs have been downselected of the Pareto front to provide an insight of the nacelle aerodynamic characteristics for medium range applications with a cruise flight Mach number of 0.80. These are the architectures with minimum $C_{D-cruise}$ (design A1), C_{D-iM} (design A2) and $C_{diversion}$ (design A3), and a trade-off design (design A4). The trade-off design was identified within the Pareto front to have the minimum cruise drag ($C_{D-cruise}$) with prescribed limits on C_{D-iM} and $C_{D-diversion}$. A summary of the different regression performance metrics for the 4 downselected designs is presented in Table 2. Relative to A1, the design A2 which has the minimum C_{D-iM} of the Pareto optimal set presents a low mid-cruise drag penalty of +0.1% and a benefit at an increase flight Mach number of -0.2%. Both designs are very near in the $C_{D-cruise}$ - C_{D-iM} space due to the strong linear correlation between both flight regimes (Figure 4b). Nonetheless, the main

difference between both architectures is their sensitivity to a diversion windmilling scenario in which the design B2 has a reduction in $C_{D-diversion}$ by -11.4% (Table 2). With respect to the aero-engine nacelle A1, the design A3 presents a benefit in $C_{D-diversion}$ of -34.2% at the expense of a drag penalty in $C_{D-cruise}$ and C_{D-iM} of +5.5% and +11.8%, respectively. Lastly, the nacelle A4 has a drag increment in $C_{D-cruise}$ and C_{D-iM} of +0.7% and +2.1% but a reduction in windmilling diversion of -27.1% (Table 2).

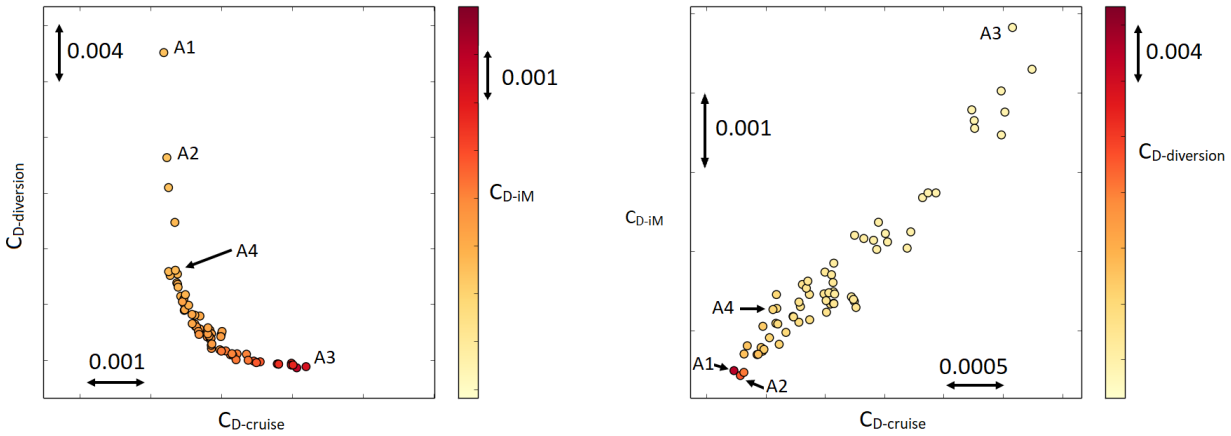

(a) $C_{D-cruise}$ - $C_{D-diversion}$ projection

(b) $C_{D-cruise}$ - C_{D-iM} projection

Figure 4 – Different projections of the Pareto front for the MOO with $L_{nac}/r_{hi} = L_{ref}$

Design	$C_{D-cruise}$	C_{D-iM}	$C_{D-diversion}$
A1	Ref.	Ref.	Ref.
A2	+0.1%	-0.2%	-11.4%
A3	+5.5%	+11.8%	-34.2%
A4	+0.7%	+2.1%	-27.1%

Table 2 – Drag performance for the 4 downselected designs within the MOO with $L_{nac}/r_{hi} = L_{ref}$

The changes in the nacelle drag characteristics are accompanied by differences in the associated flow physics. Figure 5 shows the unwrapped nacelle surface for the four downselected designs A1, A2, A3 and A4 at mid-cruise conditions. All four designs have larger peak M_{is} on the top half ($0° < \phi < 90°$) than in the bottom half ($90° < \phi < 180°$). The azimuthal location and intensity of the maximum peak M_{is} changes with the configuration. Whilst the nacelles A1 and A2 have it at the top control aero-line with $\phi = 45°$, the design A3 and A4, that have a relatively low $C_{D-diversion}$, present the peak M_{is} at $\phi = 0°$. The aero-engine nacelle A1, which has the minimum $C_{D-cruise}$, has the largest value of peak M_{is} (Figure 5). Relative to this design, the peak M_{is} reduces by 0.02, 0.06 and 0.09 for A2, A3 and A4, respectively. An initial large acceleration around the nacelle lip is usually accompanied by drag benefits because of the associated lower pressure values and, therefore, lower contributions within the drag domain. However, these flow characteristics usually depict penalties at windmilling off-design due to the concomitant stronger shock-waves that are generated. In this respect, Figure 6 shows the unwrapped nacelle surface for A1, A2, A3 and A4 at the diversion windmilling scenario. The designs A1, A2 and A4 have a large initial acceleration around the nacelle lip that terminates with a strong shock-wave. For this reason, these designs have $C_{D-diversion}$ penalties with respect to A3 (Table 2). With respect to the A1 architecture, the pre-shock Mach number reduces

by -0.08, -0.53 and -0.26 for A2, A3, A4, respectively (Figure 6).

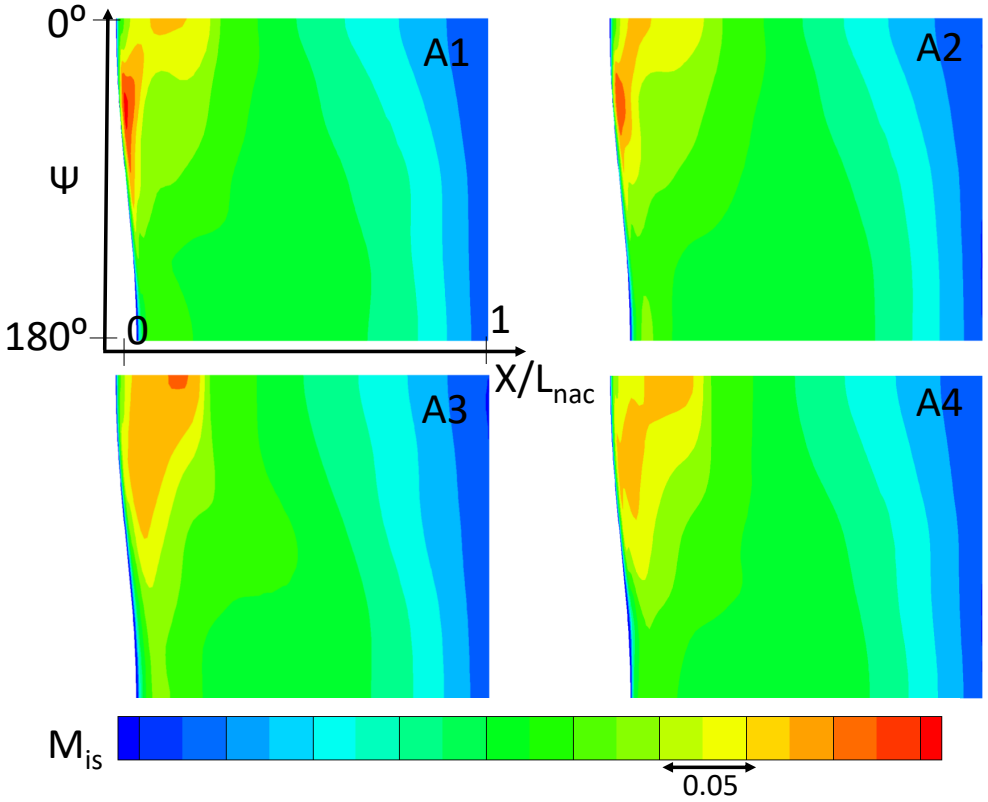

Figure 5 – Isentropic Mach number contours along the unwrapped nacelle surface (mid-cruise conditions with M = 0.8, MFCR = 0.7, AoA = 4.5°)

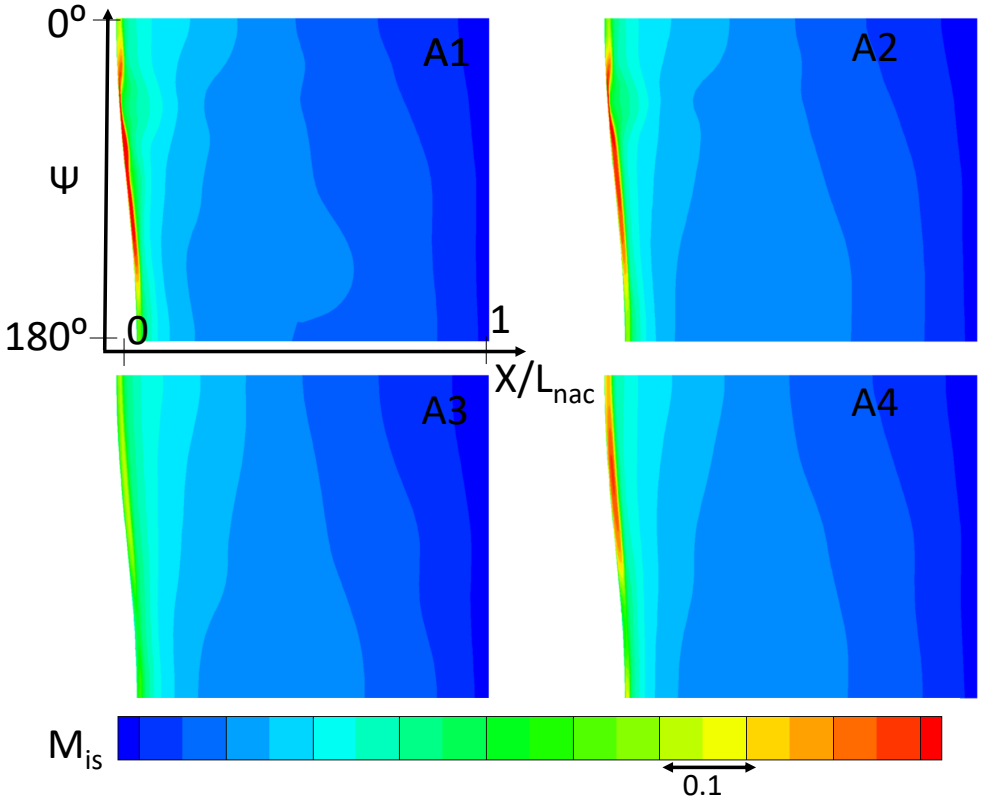

Figure 6 – Isentropic Mach number contours along the unwrapped nacelle surface (windmilling diversion scenario with M = 0.6, MFCR < 0.5, AoA = 4.5°)

Once the nacelle optimisation method was demonstrated as a suitable approach to carry multi-point, multi-objective optimisations for medium-range applications, it was deployed for compact aero-engines with $L_{nac}/r_{hi} = 0.87 \cdot L_{ref}$ and $0.81 \cdot L_{ref}$. The same numerical settings for the optimisation routine in terms of individuals per generation, operating conditions and optimisation convergence criteria were used to enable the direct comparison with the outcomes of the baseline optimisation routine with $L_{nac}/r_{hi} = L_{ref}$. The two MOOs resulted in two set of Pareto optimal sets (Figure 7). It clearly shows that relative to the reference conventional architecture, the nacelle length can be shortened to $L_{nac}/r_{hi} = 0.87 \cdot L_{ref}$ and $0.81 \cdot L_{ref}$ and there are nacelle drag benefits for the three regression objective functions considered ($C_{D-cruise}$, C_{D-iM}, $C_{D-diversion}$). It is important to highlight that the strong linear correlation between $C_{D-cruise}$ and C_{D-iM} that was identified for the reference configuration ($L_{nac}/r_{hi} = L_{ref}$) is not identified for the compact aero-engine nacelles ($L_{nac}/r_{hi} = 0.87 \cdot L_{ref}$ and $0.81 \cdot L_{ref}$). As such, the multi-point, multi-objective optimisation for compact UHBPR aero-engine nacelles should assess a flow condition at an increased flight Mach number so the Pareto front contains designs with low sensitivity to Mach number.

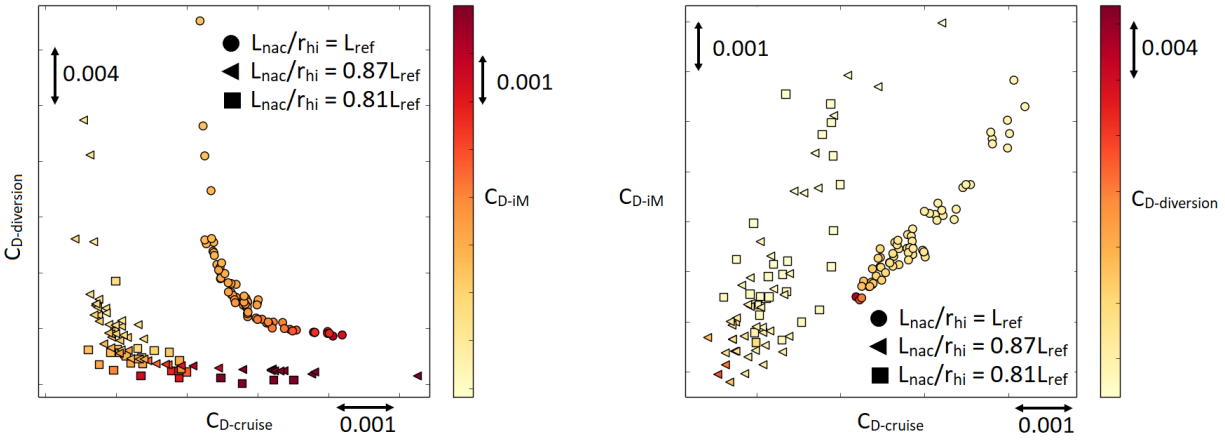

(a) $C_{D-cruise}$ - $C_{D-diversion}$ projection

(b) $C_{D-cruise}$ - C_{D-iM} projection

Figure 7 – Comparison of Pareto fronts for the MOOs with $L_{nac}/r_{hi} = L_{ref}$, $0.87 \cdot L_{ref}$ and $0.81 \cdot L_{ref}$

Following the same downselection criteria as for the baseline A4 nacelle, one nacelle from each of the two MOOs was identified. They are referred in the text as B4 and C4 for the MOO with $L_{nac}/r_{hi} = 0.87 \cdot L_{ref}$ and $0.81 \cdot L_{ref}$, respectively. Relative to the mid-cruise drag of the A4 design, a reduction of the nacelle length to $L_{nac}/r_{hi} = 0.87 \cdot L_{ref}$ results in a drag benefit of 5.8% (Figure 8). A further shortening to $L_{nac}/r_{hi} = 0.81 \cdot L_{ref}$ results in a reduction of 4.2%. As such, there is a drag penalty in mid-cruise conditions by shortening the nacelle length from $L_{nac}/r_{hi} = 0.87 \cdot L_{ref}$ to $0.81 \cdot L_{ref}$. This tendency shows that the edge of the feasible design space of UHBPR aero-engine nacelles for medium-range applications has been identified (Figure 8). Similar behavior was identified by Tejero *et al.* [21] for long-range applications in which the mid-cruise flight Mach number was 0.85. Relative to a baseline conventional nacelle with L_{nac}/r_{hi}, the reduction on nacelle length up to $L_{nac}/r_{hi} = 0.86 \cdot L_{ref}$ resulted in nacelle drag benefits. However, a further reduction on L_{nac}/r_{hi} yielded configurations with nacelle drag penalties caused by the increment on shock wave strength and its wave drag.

The M_{is} distribution along the 5 controlled aero-lines (ψ = 0°, 45°, 90°, 135° and 180°) of the 3 downselected designs (A4, B4, C4) is compared in Figure 9. It reveals differences in the peak and pre-shock M_{is}. For the top line with ψ = 0° and relative the A4 ($L_{nac}/r_{hi} = L_{ref}$), the designs B4 ($L_{nac}/r_{hi} = 0.87 \cdot L_{ref}$) and C4 ($L_{nac}/r_{hi} = 0.81 \cdot L_{ref}$) have an increment of peak M_{is} by +0.03 and +0.05, respectively. For the top-control line with ψ = 45°, the peak isentropic Mach number reduces by -0.02 for B4 and increases by +0.05 for the C4 nacelle. Nonetheless, the configuration B4 presents a well defined shock at X/L_{nac} = 0.34 which is not present in the other two designs, i.e. A4 and C4. The

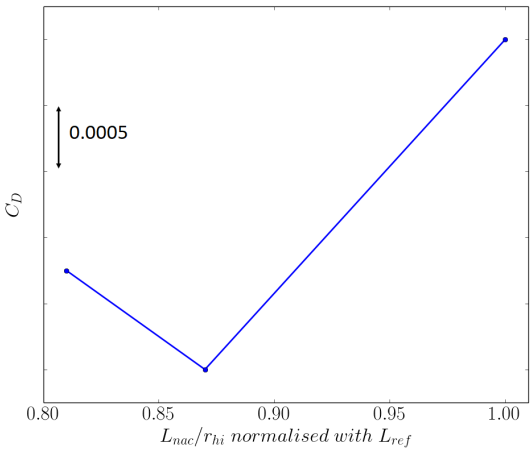

Figure 8 – Mid-cruise nacelle drag changes as a function of L_{nac}/r_{hi}

aerodynamics for the other controlled aero-lines, i.e. ψ = 90°, 135° and 180° are relatively benign and the 3 configurations have similar flow characteristics (Figure 9).

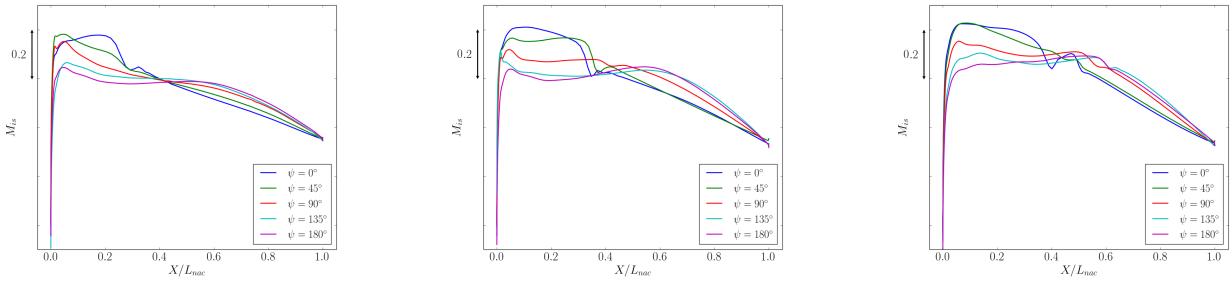

(a) $L_{nac}/r_{hi} = L_{ref}$ (b) $L_{nac}/r_{hi} = 0.87 \cdot L_{ref}$ (c) $L_{nac}/r_{hi} = 0.81 \cdot L_{ref}$

Figure 9 – Isentropic Mach number distribution along the controlled aero-lines

The baseline design A4 ($L_{nac}/r_{hi} = L_{ref}$) and the compact aero-engine B4 ($L_{nac}/r_{hi} = 0.87 \cdot L_{ref}$), which is at the edge of the feasible design space for medium range applications (Figure 8), were assessed for the sensitivity to changes in the operating conditions. Of primary interest was the effect of M, MFCR and AoA around the nominal cruise condition (Figure 10). The nacelle drag changes as a function of flight Mach number at fixed MFCR = 0.7 and AoA = 4.5° shows the larger sensitivity of compact aero-engine nacelles to increased Mach numbers (Figure 10a). For a flight Mach number below 0.82, as imposed in the optimisation for the C_{D-iM} metric, the B4 compact design has drag benefits with respect to the baseline A4 configuration. However the compact compact nacelle has drag penalties for flight Mach numbers above 0.83. At the nominal cruise M = 0.80 and AoA = 4.5°, the sensitivity of the nacelle designs to a reduction in MFCR is broadly similar for both compact and conventional configurations (Figure 10b). The drag benefits for the compact nacelle reduce with MFCR but still provides a drag benefit across the wide range of massflow capture ratio considered. Furthermore, for the nominal cruise condition with M = 0.8 and MFCR = 0.7, the nacelle drag change as a function of angle of attack was assessed. Across the range of incidences considered with 2° < AoA < 6°, the compact B4 design presents drag benefits with respect to A4. Both architectures have similar sensitivity to angle of attack (Figure 10c).

4. Conclusions

This paper has investigated the drag characteristics of compact aero-engine nacelles for medium range applications with a mid-cruise flight Mach number of 0.80. A set of different multi-point, multi-objective optimisations were carried out to identify the limits of the feasible design space for this new

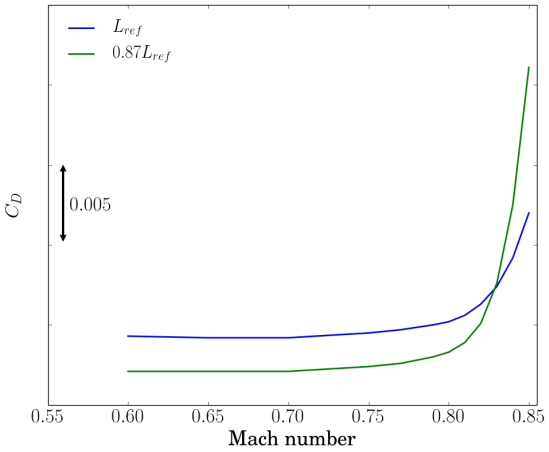

(a) Sensitivity to M at MFCR = 0.7 and AoA = 4.5°

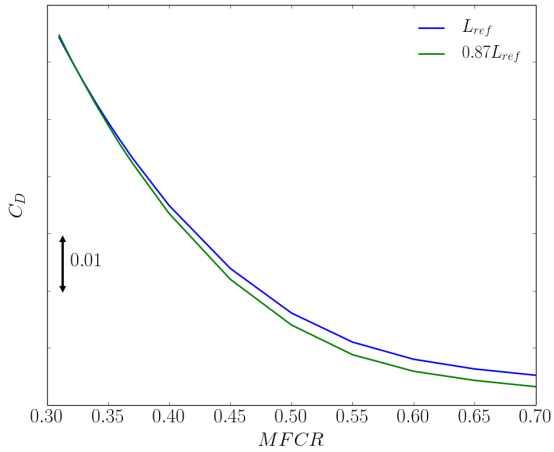

(b) Sensitivity to MFCR at M = 0.8 and AoA = 4.5°

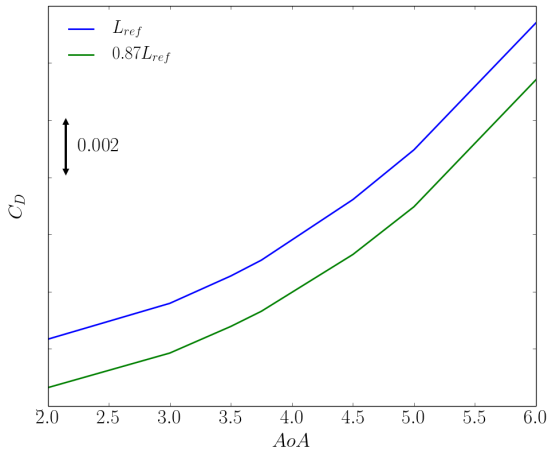

(c) Sensitivity to AoA at M = 0.8 and MFCR = 0.7

Figure 10 – Nacelle drag comparison between compact and conventional aero-engine nacelles for flight conditions within the cruise segment

design challenge. Besides, this study has quantified the expected benefits of compact UHBPR aero-engine nacelles. A well-established CFD-based method for the optimisation of aero-engine nacelles was further developed to include windmilling scenarios during the design process as well as to drive the process with regression and classification metrics.

Relative to a baseline geometry with $L_{nac}/r_{hi} = L_{ref}$, the reduction of nacelle length to $L_{nac}/r_{hi} = 0.87 \cdot L_{ref}$, results in nacelle drag benefits in the order of 5.8%. A further reduction in nacelle length to $L_{nac}/r_{hi} = 0.81 \cdot L_{ref}$ provides a drag benefit of 4.2% with respect to the reference nacelle ($L_{nac}/r_{hi} = L_{ref}$). As such, the optimal nacelle length for medium range application is at $L_{nac}/r_{hi} = 0.87 \cdot L_{ref}$. These are significantly lower benefits than the ones identified for long-range application with a mid-cruise flight Mach number of 0.85, in which for a similar shortening in nacelle length, the drag reduction was in the order of 8.5%.

5. Copyright Statement

6. Contact Author Email Address

Corresponding author: Fernando Tejero (f.tejero@cranfield.ac.uk)

7. Acknowledgment

This project has received funding from the Clean Sky 2 Joint Undertaking under the European Union's Horizon 2020 Research and Innovation Program under Grant Agreement No 820997.

References

[1] European Commission, Flightpath 2050: Europe's vision for aviation, Technical Report 978-92-79-19724-6, *Publications Office of the European Union*, 2011

[2] J.R.R.A.Martins, Aerodynamic design optimization: Challenges and perspectives, *Computers & Fluids*, Vol. 239, 105391, 2022,

[3] S.N.Skinner and H.Zare-Behtash, State-of-the-art in aerodynamic shape optimisation methods, *Applied Soft Computing*, Vol. 62, pp. 933-962, 2018

[4] M. Zhang and L. He, Combining shaping and flow control for aerodynamic optimization, *AIAA Journal*, Vol. 53, No. 4, 2015

[5] F. Tejero, P. Doerffer, O. Szulc, Shock wave induced flow separation control by air-jet and rod vortex generators, *TASK QUARTERLY*, Vol. 19, No 2, pp. 167–180, 2015

[6] S. Farokhi, Future propulsion systems and energy sources in Sustainable Aviation, *Ed: Wiley*, 2019

[7] D. Daggett, Ultra-Efficient engine technology systems integration and environmental assessment, Technical Report CR-2002-211754, NASA, 2002

[8] E. Valencia, V. Alulema, D. Rodriguez, P. Laskaridis, I. Roumeliotis, Novel fan configuration for distributed propulsion systems with boundary layer ingestion on an hybrid wing body airframe, *Thermal Science and Engineering Progress*, Vol. 18, 100515, 2020

[9] F. Sanchez-Moreno, D. MacManus, J. Hueso-Rebassa, F. Tejero, C. Sheaf, Optimization of installed compact and robust nacelles using surrogate models, *33rd Congress of the International Council of the Aeronautical Sciences*, Stockholm (Sweden), ICAS 2022

[10] I. Goulos, J. Otter, F. Tejero, J. H. Rebassa, D. MacManus, Civil turbofan propulsion aerodynamics: Thrust-Drag accounting and impact of engine installation position, *Aerospace Science and Technology*, Vol. 111, 106533, 2021

[11] F. Tejero, I. Goulos, D. MacManus, C. Sheaf, Effects of aircraft integration on compact nacelle aerodynamics, *AIAA SciTech 2020 Forum and Exposition*, AIAA Paper 2020-2225, 2020

[12] F. Tejero, M. Robinson, D. MacManus, C. Sheaf, Multi-Objective optimization of short nacelles for high bypass ratio engines, *Aerospace Science and Technology*, Vol. 91, pp. 410–421, 2019

[13] F. Tejero, R. Christie, D. MacManus, C. Sheaf, Non-axisymmetric aero-engine nacelle design by surrogate-based methods, *Aerospace Science and Technology*, Vol. 117, 106890, 2021

[14] F. Tejero, D. MacManus, J. Hueso-Rebassa, F. Sanchez-Moreno, I. Goulos, C. Sheaf, Aerodynamic optimisation of civil aero-engine nacelles by dimensionality reduction and multi-fidelity techniques, *56th 3AF International Conference AERO2022*, Toulouse, France, 28-30 March 2022.

[15] A. Savelyev, N. Zlenko, E. Matyash, S. Mikhaylov, A. Shenkin, Optimal design and installation of ultra high bypass ratio turbofan nacelle, *AIP Conference Proceedings*, Vol. 1770, 030123, 2016

[16] B. D. J. Schreiner, F. Tejero, D. MacManus, C. Sheaf, Robust aerodynamic design of nacelles for future civil aero-engines, *Proceedings of ASME Turbo Expo 2020: Turbomachinery Technical Conference and Exposition*, GT2020-14470, 2020

[17] X. Fang, Y. Zhang, S. Li, , H. Chen, Transonic nacelle aerodynamic optimization based on hybrid genetic algorithm, in: 17th AIAA/ISSMO Multidisciplinary Analysis and Optimization Conference, *AIAA AVIATION Forum*, AIAA Paper Number 2016-3833, 2016

[18] T. Simpson, T. M. Mauery, J. J. Korte, F. Mistree, Kriging models for global approximation in simulation-based multidisciplinary design optimization, *AIAA Journal*, Vol. 39, No. 12, pp. 2233–2241, 2001

[19] K. Deb, A. Pratap, S. Agarwal, T. Meyarivan A fast and elitist multiobjective genetic algorithm: NSGA-II, *IEEE Trans. Evol. Comput.*, Vol. 6, No. 2, pp. 182-197, 2002

[20] V. T. Silva, A. Lundbladh, O. Petit, C. Xisto, Multipoint aerodynamic design of ultrashort nacelles for ultrahigh-bypass-ratio engines, *Journal of Propulsion and Power*, 0, pp. 1-18, 2022

[21] Tejero F, MacManus DG, Matesanz-Garcia J, Swarthout A and Sheaf CT. Towards the design and optimisation of future compact aero-engines: intake/fancowl trade-off investigation, *56th 3AF International Conference AERO2022*, Toulouse, France, 28-30 March 2022.

[22] R. Christie, M. Robinson, F. Tejero, D. MacManus, The use of hybrid intuitive class shape transformation curves in aerodynamic design, *Aerospace Science and Technology*, Vol. 95, 105473, 2019

[23] R. Christie, A. Heidebrecht, D. G. MacManus, An automated approach to nacelle parameterisation using intuitive class shape transformation curves, *Journal of Engineering for Gas Turbines and Power*, Vol. 139, No. 6, 2017

[24] Ansys Inc., 275 Technology Drive, Canonsburg, PA 15317, ANSYS FLUENT User Guide.

[25] Ansys Inc., 275 Technology Drive, Canonsburg, PA 15317, ANSYS ICEM CFD Tutorial Manual

[26] Study Group MIDA, Guide to in-flight thrust measurement of turbojets and fan engines, in: Technical Report AGARD-AG-237, *Advisory Group for Aerospace Research and Development*, 1979

[27] F. Tejero, D. MacManus, C. Sheaf, Impact of droop and scarf on the aerodynamic performance of compact aero-engine nacelles, *AIAA SciTech 2020 Forum and Exposition*, AIAA Paper 2020-1522, 2020.

[28] F. R. Menter, Two-equation eddy-viscosity turbulence models for engineering applications, *AIAA Journal*, Vol. 32, No. 8, pp. 1598–1605, 1994

[29] Y. Jang, J. Huh, S. Lee, Y. Park, Comparative study on the prediction of aerodynamic characteristics of aircraft with turbulence models, *International Journal of Aeronautical and Space Sciences*, Vol. 19, pp. 13–23, 2018

[30] D. G. Holmes and S. D. Connell, Solution of the 2D Navier-Stokes equations on unstructured adaptive grids, AIAA Paper 89-1932-CP, *AIAA 9th Computational Fluid Dynamics Conference*, June, 1989.

[31] W. Sutherland, The Viscosity of gases and molecular force, *Philosophical Magazine*, Vol. 5, No. 35, pp. 507–531, 1893

[32] B. E. Launder and D. B. Spalding, The numerical computation of turbulent flows, *Computer Methods in Applied Mechanics and Engineering*, Vol. 3, pp. 269-289, 1974.

[33] P. Roache, A method for uniform reporting of grid refinement studies, *Journal of Fluids Engineering*, Vol. 116, No.3, pp. 405–413, 1994

[34] J. C. Helton, F. J. Davis, Latin hypercube sampling and the propagation of uncertainty in analyses of complex systems, *Engineering and System Safety*, Vol. 81, pp. 23–69, 2003

[35] W. Hoelmer, J. L. Younghans, J.C. Reynal, Effect of Reynolds number on upper cowl flow separation, *Journal of Aircraft*, Vol. 24, No. 3, pp. 161-169, 1987

[36] A. Auger, J. Bader, D. Brockhoff, E. Zitzler, Hypervolume-based multiobjective optimization: theoretical foundations and practical implications, *Theoretical Computer Science*, Vol. 425, pp. 75–103, 2012